Available online at www.sciencedirect.com
ScienceDirect
Geochimica et Cosmochimica Acta 75 (2011) 1145–1160
Geochimica et Cosmochimica Acta
www.elsevier.com/locate/gca

Plume–ridge interaction along the Galapagos Spreading Center: discerning between gas loss and source effects using neon isotopic compositions and ^4He–$^{40}Ar^*$–CO_2 relative abundances

A. Colin [a,*], P.G. Burnard [a], D.W. Graham [b], Y. Marrocchi [a]

[a] Centre de Recherches Pétrographiques et Géochimiques, CNRS UPR 2300, 15 rue Notre-Dame des Pauvres, BP20, 54501 Vandoeuvre-lès-Nancy Cedex, France
[b] College of Oceanic & Atmospheric Sciences, Oregon State University, Corvallis, OR 97331, USA

Received 30 June 2010; accepted in revised form 4 October 2010; available online 25 November 2010

Abstract

To document the plume–ridge interaction at the Galapagos Spreading Center (GSC), we present neon 3-isotope analyses performed on vesicles-trapped volatiles of MORB glasses dredged along the ridge axis between 86°W and 98°W. ^4He–$^{40}Ar^*$–CO_2 relative abundances were also measured in order to study gas loss in this context and discern between source and degassing effects. Neon isotopic compositions are in the MORB range with $^{21}Ne/^{22}Ne$ ratios extrapolated to the $^{20}Ne/^{22}Ne$ mantle ratio of 12.5 varying between 0.053 and 0.072. Unradiogenic plume-like compositions were not measured. The ^4He–$^{40}Ar^*$–CO_2 relative abundances are highly variable along the ridge, for example $^4He/^{40}Ar^*$ ratio varies between 3 and 433, but these variations can be fully explained by a simple model of Rayleigh distillation, with a single volatile source composition for the entire GSC. Magma fractional crystallisation, which increases in the plume influenced zone, seems to be the main motor for degassing. As other geochemical and geophysical studies indicate a significant plume influence on the GSC, these results suggest the plume component feeding the ridge is either degassed or else different from the plume core.

1. INTRODUCTION

1.1. Study objectives

About 15–20% of the mid-oceanic ridge system is affected by plumes (Ito et al., 2003). These ridge areas sample material from two different reservoirs and we can thereby study the influence of plumes on magmatic processes resulting in changes in geodynamic and physical parameters of the ridge. Studying volatiles, including the noble gases, in plume-affected ridges is particularly interesting as (1) the different mantle reservoirs have distinct noble gases isotopic signatures, which permit the respective plume and mid-oceanic ridge basalts (MORB) mantle contributions to be estimated and allow mantle reservoir mixing processes to be investigated, (2) "abnormal" sections of ridges are ideal natural laboratories for examining the parameters influencing degassing processes because the plume interactions often lead to systematic variations in bathymetry, temperature and melt supply and (3) corrections for degassing can permit mantle volatile composition heterogeneity to be assessed and so improve our knowledge of the fractionation processes.

Numerous recent works (morphological, geophysical and geochemical studies) have improved our knowledge of the Galapagos plume characteristics and its influence on the Galapagos Spreading Center (GSC) in the eastern equatorial Pacific (e.g. the G-PRIME project, Detrick et al., 2002). Sr, Nd, Pb and Hf isotopic ratios evolve systematically along the GSC from 91°W, the area of peak influence of the Galapagos hotspot, to values typical of local depleted mantle east and west of 91°W (Schilling et al., 2003). Calculations by these authors show a 30% plume component contribution at 91°W. However, an

* Corresponding author.
E-mail address: acolin@crpg.cnrs-nancy.fr (A. Colin).

0016-7037/$ - see front matter © 2010 Elsevier Ltd. All rights reserved.
doi:10.1016/j.gca.2010.11.018

exception to these compositional variations are helium isotopes, usually considered as among the most sensitive tracers of plume material to MOR, yet $^3He/^4He$ varies little along the GSC (Detrick et al., 2002). The difference in helium isotopic composition between plumes and MORB has been used with success to estimate plume dimensions and shallow dispersion for example in Iceland (Kurz et al., 1985; Breddam et al., 2000) and along the EPR (Kurz et al., 2005). Indeed, MORB helium isotopic compositions are homogeneous with $^3He/^4He$ around 8 Ra (atmospheric ratio). Ratios in OIB are generally less radiogenic, up to 50 Ra (Iceland – Starkey et al., 2009), and are more variable (Graham, 2002). Basalts from Fernandina, the island considered to be closest to the Galapagos plume center present extremely unradiogenic helium isotope compositions (Graham et al., 1993; Kurz and Geist 1999; Kurz et al., 2009) with $^3He/^4He$ ratios up to 29 Ra. Extremely unradiogenic neon was also measured in Fernandina (Kurz et al., 2009). However, there is a strong decrease in $^3He/^4He$ away from Fernandina (8.6 Ra in Santa Cruz and 6.9 Ra in Pinta islands) (Kurz and Geist, 1999; Kurz et al., 2009), thought to be due to preferential depletion of He from the plume material during melting, or to a heterogeneous plume, and the same is suspected for neon, because MORB-like composition have been measured in the north, at Wolf volcano (Kurz et al., 2009). Although a peak in $^3He/^4He$ is observed on the GSC, co-incident with the peak in Sr, Nd, Pb and Hf, all $^3He/^4He$ ratios over the entire length of the GSC are within the MORB range, varying from 5.9 to 8.5 Ra (Detrick et al., 2002).

This contribution presents analyses of vesicle-trapped volatiles in MORB glasses along the plume influenced zone of the GSC between 86°W and 98°W. Neon isotopic analyses are used to assess if this "decoupling" between lithophile isotopes and helium affects all volatiles or is due to a particular behaviour of helium. As degassing processes fractionate volatiles according to their respective solubilities or diffusivities, the direct or indirect influence of plume on degassing intensities and mechanisms are also examined by the study of ^4He–$^{40}Ar^*$–CO_2 relative abundances.

1.2. Geological background

The GSC, in the central east Pacific, is located about 200 km north of the Galapagos archipelago (Fig. 1). Numerous geophysical, geochemical and volcanological parameters show a clear influence of the plume on the ridge (Detrick et al., 2002). As the ridge approaches the plume, spreading rates change from 45 mm/y west of 98°W to 56 mm/y near 91°W and the axial depth decreases abruptly from 3500 m to less than 1700 m (Ito and Lin, 1995). Seismic data show that the crust thickens by 2.3 km between 97°W and 91.25°W, and the top of the axial magma chamber (AMC) passes from 2.5 to 4.25 km below the surface west of 92.7°W to 1.38 to 2.25 km east of 92.7°W (Detrick et al., 2002). At the same location, gravity data show a decrease in mantle Bouguer anomaly (MBA) of about 70 mGal. Part of the MBA and topographic swell between 91°W and 98°W is not explained by crustal thickness variations (Canales et al., 2002; Detrick et al., 2002). This excess buoyancy can be explained either by melt retention beneath the ridge or by transport of depleted plume residuum (following melting beneath the Galapagos Islands) toward the GSC (Canales et al., 2002). Shoaling of the AMC is accompanied by a decrease in $MgO/(MgO + FeO)$ due to increased fractional crystallisation (Detrick et al., 2002). The concentration of incompatible elements increases in the plume influenced zone, interpreted as the arrival of plume source material rich in incompatible elements (Schilling et al., 1976, 1982; Fisk et al., 1982; Verma and Schilling, 1982; Verma et al., 1983). Na_8 and Ca_8/Al_8 (corrected for crystallization to $MgO = 8$) increase east of 92.7°W, which is probably due to a lower melting rate in the plume influenced zone. However as melt supply increases (as indicated by the thickened crust), this must be the result of a low partial melting rate of a larger volume of mantle, thought to be hydrated in order to reduce the melting temperature (Detrick et al., 2002). However, quantitative interpretation of these chemical variations along the GSC in terms of plume contribution are complex as the Galapagos islands themselves are known to be heterogeneous with respect to Sr–Nd–Pb isotopic compositions (Schilling et al., 2003), and to helium isotopic compositions (Kurz and Geist, 1999; Kurz et al., 2009). This variability is often explained by multi-component mixing and a heterogeneous plume.

1.3. Samples and analytical techniques

Twenty one glassy submarine basalts dredged by Sonne 158 and Ewing Cruise 4 between 86°W and 98°W along the GSC were analysed. Major element chemistry for these samples is reported in Christie et al. (2005) along the eastern GSC and by Cushman et al. (2004) along the western GSC (Fig. 1). Helium isotopic ratios for a subset of the samples have been measured at NOAA following the method described by Graham et al. (1998); part of the data have already been published in Detrick et al. (2002) between 92.7°W and 94°W, and we report in Table 2 few new high-precision helium isotope ratios.

For the present analyses, the largest possible fragments of fresh glass were selected. Samples were sonically cleaned in acetone, and heated under ultra-high vacuum for 12 h at about 100 °C, and then pumped about 6 h at ambient temperature in order to reduce air adsorption on sample surfaces.

Volatiles contained in the vesicles of the glass samples were extracted in several crushing steps in vacuo. Due to the low vesicularity of these GSC glasses, three chips of about 500 mg each of a single sample were crushed simultaneously. During crushing, the pressure in the line was measured using a capacitance manometer (Pfeiffer baratron type CMR 262). Previous studies have shown that the pressure increase during crushing is due to gases released from the vesicles, mostly CO_2 which is the dominant gas in MORB vesicles (Barker and Torkelson, 1975; Moore, 1979; Javoy and Pineau, 1991). Using pressure as an indicator of the quantity of gases released, crushing was stopped when the quantity of gas was deemed sufficient for the analyses. In general, three or four crushing steps were

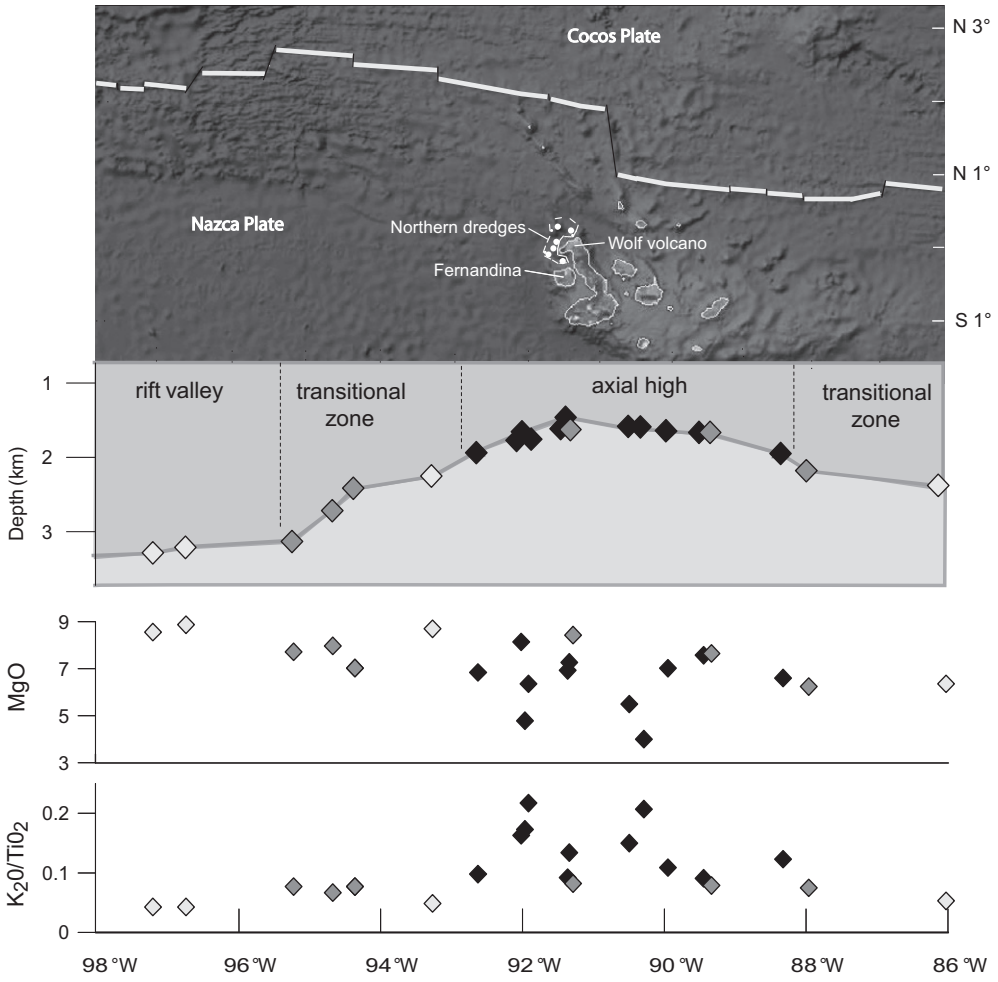

Fig. 1. Location along the GSC between 86°W and 98°W of the 21 glass samples analysed here and ridge bathymetry, MgO, K_2O/TiO_2 content of basalts (after Cushman et al., 2004; Christie et al., 2005). The GSC is shown in yellow on the map. The Galapagos Islands can be discerned on the Nazca Plate. Northern dredges analyzed by Kurz et al. (2009) were localized at the white points in the dashed area. Black, gray and white diamonds represent, respectively E-MORB (K/Ti > 0.15), T-MORB (0.09 < K/Ti < 0.15), and N-MORB (K/Ti < 0.09). K/Ti cut-off values used to define E-, T- and N-MORB are after Detrick et al. (2002).

performed in order to extract all the gas from the samples. The first crushing step was very short (between 2 and 30 impacts) in order to open only the largest vesicles. In the final step, crushing was stopped when the pressure no longer increased during crushing in order to avoid gases released from the glass (as opposed to from the vesicles), and to avoid noble gas adsorption on a fine grained sample powder (Barker and Torkelson, 1975; Burnard et al., 2002). The CO_2 content was directly estimated from the pressure increase within a calibrated volume.

Gases were subsequently purified with titanium getters, in order to remove CO_2 and other active gases. Ar was trapped and isolated in an activated charcoal finger held at liquid nitrogen temperature, and then neon was adsorbed onto a stainless steel grid cooled to 30 K. At this stage, helium remained as a free gas in the purification line. Analyses were performed on a Helix Multi Collection mass spectrometer. ^{4}He was first measured using a faraday cup. Then the neon was desorbed from the steel grid at 60 K and the three neon isotopes measured by multi-collection. ^{22}Ne was corrected for CO_2^{++} contributions following Marrocchi et al. (2009); mass spectrometer resolution was sufficient to separate ^{20}Ne from $^{40}Ar^{++}$ therefore no correction was required (see Marrocchi et al. (2009) for further details). ^{40}Ar and ^{36}Ar were then measured by peak jumping. The blanks were under the detection limit for ^{4}He and ^{20}Ne, that means lower than 3×10^{-14} moles and 5×10^{-17} moles, respectively, therefore no blank correction was applied for these two elements. Moreover neon blanks are probably atmospheric, thus correction of neon data from atmospheric contamination will include correction from blank. Blanks for argon were atmospheric, between 1 and 3×10^{-14} moles, and have been corrected in order to calculate the true $^{40}Ar/^{36}Ar$ ratio of the samples. Neon and argon standards were aliquots of air and the helium standard is a volcanic gas from Reunion, characterised by $^3He/^4He$=12.4 Ra; the sizes of the standards were varied to bracket the sample concentrations.

2. RESULTS

The He and CO_2 abundances and the Ne and Ar abundances and isotopes are reported in Table 1. Samples present low gas concentrations (2.38×10^{-8} mol $g^{-1} < [CO_2] < 3.22 \times 10^{-6}$ mol g^{-1}). $^{40}Ar/^{36}Ar$ ratios vary between 309 and 12,300, but most of the samples present significant atmospheric contamination, particularly between 89°W and 92°W (the axial high) where all samples present $^{40}Ar/^{36}Ar$ ratios lower than 610 with the exception of sample SO47-A.

As a result of this contamination, neon isotopic ratios are close to atmospheric on the axial high, with $^{20}Ne/^{22}Ne < 10.5$ between 89°W and 95°W which precludes accurate correction of the isotopic ratios for atmospheric contamination in this area. However, samples in general plot around the MORB mantle source – air mixing line in a Ne 3-isotopes plot (Fig. 2). Note some samples present $^{20}Ne/^{22}Ne$ lower than the atmospheric ratio. The noble gas relative abundances were also measured along the GSC. When corrected for atmospheric contamination, relative abundances vary widely. For example $^{4}He/^{40}Ar^{*}$ (where $^{40}Ar^{*}$ represents ^{40}Ar corrected for atmospheric contamination on the basis that all ^{36}Ar is atmospheric in origin) varies from 3 to 433, with maximum values in the axial high. The inverse applies to the $^{40}Ar^{*}/CO_2$ ratio (4.9×10^{-8}–3.8×10^{-5} with minimum values in the axial high) and which anticorrelates well with $^{4}He/^{40}Ar^{*}$. These results confirm that the GSC has undergone variable degassing and therefore is an appropriate area to study relative contributions of degassing and source mixing on noble gases composition.

2.1. Neon isotopic compositions along the GSC

As in most geological samples, the Ne isotopic compositions of our samples lie along mixing lines due to atmospheric contamination, one end of which is defined by the atmospheric composition and the other end corresponding to the sample composition. In mantle samples, helium isotopic ratios frequently correlate with the slope of the line in the neon three isotope graph (e.g. Moreira and Sarda, 2000; Moreira et al., 2001; Kurz et al., 2009). In these two isotopic systems, ^{3}He, ^{20}Ne and ^{22}Ne are considered to be inherited from the earth's initial volatile budget as they are not produced in significant quantities within the earth. ^{4}He and ^{21}Ne are radiogenic, genetically linked because ^{4}He is produced by Th and U decay, and this same decay produces ^{21}Ne via the indirect reaction $^{18}O(\alpha, n)^{21}Ne$ resulting in a constant mantle $^{4}He/^{21}Ne$ production ratio of 2.2×10^{7} (Yatsevich and Honda, 1997). As $^{20}Ne/^{22}Ne$ is considered to be homogeneous in the whole mantle, $^{21}Ne/^{22}Ne_{extrap}$ (the ratio corrected for air contamination) can be calculated by extrapolating from the air composition to the $^{20}Ne/^{22}Ne$ ratio of the mantle (normally considered to be either 12.5 or 13.8 (Niedermann et al., 1997; Moreira et al., 1998; Yokochi and Marty, 2004). All the ratios reported here are extrapolated to $^{20}Ne/^{22}Ne$ mantle ratio of 12.5, including literature data which have been recalculated to this mantle value for consistency.

Two of our samples clearly have $^{20}Ne/^{22}Ne$ ratios lower than the atmospheric pole; this is unlikely to be an analytical artefact because the mass spectrometer resolves the $^{40}Ar^{++}$ isobar on ^{20}Ne (Marrocchi et al 2009). Possibly these results are due to the release of a fractionated component (by diffusion?) from the glass during crushing. However, it is also plausible that the atmospheric contaminant was mass fractionated during the contamination process, for example the residue of a phase separation process (of seawater) which induced kinetic isotope fractionation could produce neon with $^{20}Ne/^{22}Ne$ ratios lower than air. Whatever the mechanism, this seems to be a relatively rare phenomenon as most of our contaminated samples plot close to the air pole.

Our Ne data pattern is consistent with the He isotope distribution, notably in that unradiogenic (Galapagos plume-like, Kurz et al., 2009) compositions are not present on the GSC, and all $^{21}Ne/^{22}Ne_{extrap}$ are close to the value deduced from the MORB – air mixing-line (Sarda et al., 1988; Moreira et al 1998). This confirms the tendency observed by Kurz et al. (2009) who observe a rapid decrease in the unradiogenic Ne plume signal away from Fernandina. Neither neon nor helium isotopic ratios show a strong plume signal along the GSC, and therefore both He and Ne isotopic compositions seem to be controlled by a single mechanism as opposed to different processes independently influencing the Ne and He isotopic compositions. The nature of this mechanism is discussed in the following paragraphs.

Nevertheless, GSC samples present a range of $^{21}Ne/^{22}Ne_{extrap}$ compositions clustering around the MORB line, with ratios varying between 0.053 and 0.072 (Fig. 2). The subtle variations in $^{21}Ne/^{22}Ne_{extrap}$ observed here contrast sharply with the large variations observed on the East Pacific Rise at 17°S, which are associated with a much smaller geochemical and geophysical anomaly (Kurz et al., 2005). However we can expect these variations to reflect source variations due to mixing between the MORB reservoir and the unradiogenic plume component.

Mixing can be studied in a Ne vs. He isotopic diagram, with the advantage that the isotope ratios are not sensitive to fractionation by degassing. In Fig. 3 we report our data alongside those of Kurz et al. (2009). To explain the He and Ne compositions of the Northern dredges (cf. Fig. 1 for location), Kurz et al. (2009) propose mixing between plume and MORB end-members. Consistent with the low $^{3}He/^{4}He$ ratios measured along the GSC (these data; Detrick et al, 2002), we observe $^{21}Ne/^{22}Ne_{extrap}$ that are higher than for typical MORB (e.g. for a mantle $^{20}Ne/^{22}Ne$ ratio of 12.5, typically $^{21}Ne/^{22}Ne_{extrap} = 0.06$) demonstrating that, as for He isotopes, there is not a single $^{21}Ne/^{22}Ne$ ratio for the convecting mantle.

In a plot of $^{20}Ne/^{22}Ne$ vs. $^{3}He/^{22}Ne$ (Fig. 4, after Kurz et al., 2009) the data define mixing lines between air and a mantle reservoir. $^{3}He/^{22}Ne_{extrap}$ seems to increase with distance from Fernandina with values of about 1 for Fernandina, 10 in the Northern dredges (Kurz et al., 2009) and more variable but around 20 in the GSC (this study). $^{3}He/^{22}Ne_{extrap}$ needs to be considered in the context of both plume-MORB mixing and He–Ne fractionation. As

Table 1
Neon isotopes and Ar–^{4}He–CO_2 abundances in GSC basaltic glasses.

Sample name	Long W	Weight (g)		CO_2	σ	^{4}He	σ	^{40}Ar	σ	^{40}Ar/^{36}Ar	σ	^{4}He/^{40}Ar*	σ	^{20}Ne	σ	^{21}Ne/^{22}Ne	σ	^{20}Ne/^{22}Ne	σ
				$\times10^{-3}$ (mol g^{-1})		$\times10^{-12}$ (mol g^{-1})		$\times10^{-12}$ (mol g^{-1})						$\times10^{-16}$ (mol g^{-1})		$\times10^{-2}$			
SO 3-1B	86.0		Crush 1	4.3	0.3	9.1	0.2	1.2	0.1	1145	23	10.1	0.7	b. d.	–	b. d.	–	b. d.	–
			Crush 2	6.8	0.5	21.7	0.5	3.5	0.2	1162	23	8.5	0.6	8.8	0.4	3.28	0.05	9.99	0.08
		1.88	*Total*	11	0.6	30.7	0.5	4.7	0.2	1157	23	8.9	0.5						
SOD17-2B	88.0		Crush 1	106.1	0.8	80.5	1.9	7.3	0.2	2502	50	12.5	0.6	17.0	0.9	3.62	0.05	10.62	0.08
			Crush 2	125	1	110	3	9.1	0.3	10202	204	12.5	0.5	9.0	0.5	4.85	0.07	11.98	0.09
		1.22	*Total*	231	1	190	3	16.4	0.4	4298	86	12.5	0.4	26	1				
SO-D19	88.3		Crush 1	n. a.	–	31	1	1.3	0.0	1003	20	35	2	b. d.	–	b. d.	–	b. d.	–
			Crush 2	163	4	117	4	7.2	0.2	1050	21	23	1	29.8	0.5	3.39	0.05	10.19	0.06
			Crush 3	128	3	98	4	2.8	0.1	3845	77	38	2	8.4	0.2	4.49	0.07	11.64	0.07
		1.30	*Total*	–	–	246	6	11.3	0.2	1272	25	28	1						
SOD26-2B	89.3		Crush 1	31.5	0.2	18.7	0.4	4.4	0.1	437	9	13	2	43	2	2.99	0.04	9.82	0.07
			Crush 2	25.4	0.4	19.4	0.4	2.0	0.1	1289	26	12.9	0.6	12.5	0.7	3.22	0.04	10.22	0.08
		1.45	*Total*	57	0.5	38.1	0.6	6.4	0.2	547	11	13.1	0.9	55	2				
SOD27A-1	89.4		Crush 1	69.2	0.8	52	1	8.6	0.3	607	12	12	0.9	61	3	3.00	0.01	9.77	0.07
			Crush 2	39.5	0.9	34.7	0.8	4.7	0.2	620	12	14	1	37	2	2.99	0.01	9.83	0.07
		1.15	*Total*	109	1	87	1	13.3	0.3	611	12	12.8	0.7	98	4				
SO33-2B	89.9		Crush 1	45	14	17.1	0.4	5.4	0.2	350	7	22	7	65	4	2.89	0.01	9.6	0.1
			Crush 2	21.6	0.8	7.7	0.2	1.6	0.1	447	9	15	2	14.4	0.8	2.71	0.01	9.0	0.1
		0.95	*Total*	67	14	24.8	0.4	7.0	0.2	368	7	19	4	79.0	3.6				
SOD35-1	90.3		Crush 1	15	0.9	1.5	0.0	0.344	0.01	282	6	INF		4.5	0.2	3.15	0.07	9.5	0.2
			Crush 2	36.6	0.9	22.5	0.2	2.94	0.05	457	9	22	1	17.2	0.7	2.96	0.06	10.1	0.2
			Crush 3	b. d.	–	4.4	0.0	0.83	0.01	348	7	43	7	8.2	0.3	2.94	0.06	*	
		1.41	*Total*	–	–	28.4	0.2	4.11	0.05	410	8	26	1	29.9	0.8				
SOD36-5	90.5		Crush 1	48.3	0.7	28.1	0.2	1.31	0.02	556	11	47	2	7.1	0.3	3.32	0.07	9.2	0.2
			Crush 2	66.9	4.0	42.3	0.3	n. a.	–	n.a.	–	–	–	6.5	0.3	3.41	0.07	10.2	0.2
		1.50	*Total*	115.3	4.0	70.5	0.4							13.7	0.4				
SO 47A	91.3	2.64	Crush	2.4	1.4	4.8	0.1	n.a.		2180	44	–	–	b. d.	–	b. d.	–	b. d.	–
SO 48-6	91.3	2.09	Crush	9.5	3.5	n.a.		n.a.		370	7	–	–	9.4	0.2	3.47	0.05	10.2	0.1
SO 53-1	91.9		Crush 1	94.7	0.3	43.5	0.5	9	0.5	342	7	39	25	89	4	2.98	0.04	9.92	0.06
			Crush 2	73.6	0.5	33.9	0.4	4.7	0.2	359	7	44	20	26	1	2.97	0.04	9.78	0.06
			Crush 3	40	1	25.8	0.3	1.4	0.1	513	10	45	7	10.5	0.5	3.10	0.04	9.65	0.06
		1.80	*Total*	208	1	103.2	0.7	15.1	0.5	358	7	42	14	126	5				
EW 9-1	91.4		Crush 1	45.6	0.3	32.1	0.7	3.0	0.1	348	7	78	27	30	2	2.92	0.03	9.81	0.05
			Crush 2	34.2	0.3	25.9	0.5	2.0	0.1	363	7	74	21	20	1	3.01	0.03	9.85	0.05
			Crush 3	50.9	0.4	43.2	0.9	2.1	0.1	444	9	64	9	17.7	0.9	3.08	0.03	9.81	0.05
		1.65	*Total*	130.6	0.6	101	1	7.1	0.2	376	8	71	10	68	2				
EW 19-1	92.0		Crush 1	31	1	22	1	7.3	0.4	310	6	83.6	[25-INF]	48	3	2.86	0.03	9.4	0.1
			Crush 2	21.2	0.6	n. a.	–	n. a.	–	n.a.	–	–	–	8.3	0.6	2.93	0.03	8.7	0.1
		1.65	*Total*	52	1									56	3				

(*continued on next page*)

Table 1 (*continued*)

Sample name	Long W	Weight (g)		CO_2	σ	^4He	σ	^{40}Ar	σ	$^{40}Ar/^{36}Ar$	σ	$^4He/^{40}Ar^*$	σ	^{20}Ne	σ	$^{21}Ne/^{22}Ne$	σ	$^{20}Ne/^{22}Ne$	σ
				$\times10^{-3}$ (mol g^{-1})		$\times10^{-12}$ (mol g^{-1})		$\times10^{-12}$ (mol g^{-1})						$\times10^{-16}$ (mol g^{-1})		$\times10^{-2}$			
EWD20-1B	92.0		Crush 1	114.3	0.5	28.4	0.7	3.2	0.1	304	6	506.7	[130-INF]	46	3	2.96	0.04	9.77	0.07
			Crush 2	144	1	48	1	2.4	0.1	315	6	398.9	[200-INF]	32	2	3.00	0.04	9.74	0.07
		1.53	*Total*	258	2	76	1	5.6	0.1	309	6	433.3	[202-INF]	79	3				
EW 29-1	92.6		Crush 1	70.8	0.4	31.8	0.9	3.4	0.1	430	9	31	3	28	2	3.07	0.03	10.04	0.04
			Crush 2	61.3	0.3	29.4	0.8	2.09	0.04	2072	41	17	1	5.3	0.3	n.a.	–	n. a.	–
		1.62	*Total*	132.1	0.5	61	1	5.5	0.1	616	12	22	1	33	2				
EW 29-1r	92.6		Crush 1	101.0	0.3	42.9	0.9	n. a.	–	n. a.	–	–	–	247	12	2.76	0.04	9.86	0.08
Second analysis			Crush 2	67.5	0.4	32.4	0.7	3.0	0.1	1146	23	15	1	n. a.	–	n. a.	–	n. a.	–
			Crush 3	138	1	69	1	7.9	0.4	2818	56	9.8	0.6	9.5	0.5	3.70	0.05	10.30	0.08
		1.42	*Total*	306	1	144	2												
EW43-1B	93.3		Crush 1	100.2	0.4	35.1	0.8	14	0.5	3370	67	2.8	0.1	17.0	0.9	3.50	0.01	10.18	0.07
			Crush 2	102.3	0.8	25.1	0.6	11.1	0.4	1835	37	2.7	0.1	18	1	3.31	0.01	10.09	0.07
			Crush 3	95.1	0.5	33.0	0.8	11.7	0.4	4106	82	3.0	0.1	11.6	0.6	3.74	0.01	10.54	0.07
		1.48	*Total*	298	1.0	93	1	36.7	0.7	2821	56	2.8	0.1	47	2				
EW 58-2	94.4		Crush 1	62.5	0.3	26.7	0.6	6.2	0.2	580	12	8.9	0.8	40	2	3.07	0.03	9.98	0.06
			Crush 2	56.5	0.3	29.0	0.6	6.9	0.3	497	10	11	1	43	2	3.01	0.03	9.91	0.06
			Crush 3	81	0.3	41.4	0.9	6.2	0.2	1058	21	9.4	0.6	31	2	3.21	0.03	10.06	0.06
			Crush 4	58.2	0.3	32.2	0.7	3.6	0.1	1201	24	12.0	0.7	21	1	3.13	0.03	9.91	0.06
		1.99	*Total*	258.2	0.6	129	1	22.9	0.5	684	14	10.1	0.2	135	3				
EW 58-2r	94.4		Crush 1	78.2	0.4	36.8	0.8	6.6	0.3	745	15	9.3	0.8	36	2	3.06	0.04	9.93	0.08
second analysis			Crush 2	58.2	0.3	29.2	0.6	4.2	0.2	1365	27	8.9	0.6	16.5	0.8	3.19	0.05	10.11	0.08
			Crush 3	77	0.3	39.3	0.8	5.3	0.3	1694	34	9.1	0.6	18.5	0.9	3.27	0.05	10.17	0.08
		1.95	*Total*	213.5	0.6	105	1	16.1	0.5	1067	21	9.1	0.4	71	2				
EW 62-5B	94.7		Crush 1	–	–	5.4	0.2	1.10	0.02	6103	122	5.1	0.2	b. d.	–	b. d.	–	b. d.	–
			Crush 2	19	2	12.3	0.4	2.7	0.1	4232	85	4.9	0.2	b. d.	–	b. d.	–	b. d.	–
			Crush 3	38	2	33	1	9.6	0.2	2275	45	3.9	0.1	b. d.	–	b. d.	–	b. d.	–
		2.20	*Total*			51	1	13.5	0.2	2660	53	4.2	0.1						
EW 69-1	95.2		Crush 1	86.4	0.2	37.3	0.9	5.7	0.1	13796	276	6.8	0.2	3.7	0.3	5.35	0.05	11.34	0.05
			Crush 2	118	5	50	1	8.1	0.2	12950	259	6.3	0.2	6.1	0.5	4.95	0.04	11.10	0.05
			Crush 3	117.6	0.8	52	1	8.0	0.2	10993	220	6.6	0.2	6.0	0.5	5.22	0.05	11.28	0.05
		2.31	*Total*	322	5	139	2	21.8	0.3	12338	247	6.6	0.1	15.7	0.7				
EW 79 1	96.7		Crush 1	23.9	0.9	25.8	0.8	6.3	0.1	4620	92	4.4	0.2	4.8	0.2	3.99	0.05	10.9	0.1
			Crush 2	4.8	0.4	7.3	0.2	1.97	0.04	1257	25	4.9	0.2	5.9	0.2	3.40	0.04	9.7	0.1
		1.86	*Total*	29	1	33	0.8	8.3	0.1	2819	56	4.5	0.1	10.7	0.3				
EW 88-1	97.2		Crush 1	58.5	0.6	26.9	0.7	11.6	0.3	2164	43	2.7	0.1	20	2	3.21	0.03	9.89	0.04
			Crush 2	71.9	0.5	34.2	0.9	9.2	0.2	4367	87	4.0	0.1	16	1	3.39	0.03	10.08	0.04
			Crush 3	96.8	0.4	46	1	12	0.3	8356	167	4.0	0.1	12	1	3.96	0.03	10.53	0.05
		2.11	*Total*	227.2	0.8	107	2	32.8	0.5	3685	74	3.6	0.1	48	2				

b.d.: below detection; n.a.: not analysed; INF: infinity. *: Analysis gives $^{20}Ne/^{22}Ne = 7.7$, this result is not reported in the table as we think it is due to an analytical problem.

Table 2
Helium isotopes analyses in GSC basaltic glasses.

Sample name	Long °W	He mol/g	$^3He/^4He$	$2 \times \sigma$
SO 3-1B	86.0	1.54E-10	8.51	0.05
SOD17-2B	88.0	2.75E-10	8.26	0.06
SO-D19	88.3	2.94E-10	8.29	0.05
SOD26-2B	89.3	4.20E-11	8.33	0.05
SOD27A-1	89.4	1.87E-10	7.77	0.04
SO33-2B	89.9	3.33E-11	8.04	0.05
SOD35-1	90.3	4.87E-11	7.84	0.05
SOD36-5	90.5	1.09E-10	7.62	0.05
SO 47A	91.3	5.54E-11	8.06	0.05
SO 48-6	91.3	6.29E-11	8.23	0.06
SO 53-1	91.9	1.37E-10	7.25	0.04
EW 9-1*	91.4	1.63E-10	8.07*	0.04*
EW 19-1*	92.0	7.77E-11	7.55*	0.04*
EWD20-1B*	92.0	1.38E-10	8.05*	0.04*
EW 29-1*	92.6	2.79E-10	7.38*	0.04*
EW43-1B	93.3	1.93E-10	6.9	0.04
EW 58-2	94.4	2.15E-10	6.99	0.04
EW 62-5B	94.7	1.72E-10	5.92	0.03
EW 69-1	95.2	9.69E-11	7.22	0.04
EW 79 1	96.7	6.52E-11	6.36	0.03
EW 88-1	97.2	2.66E-10	7.2	0.04

* Analyses already published in Detrick et al. (2002).

suggested by Kurz et al. (2009), the $^3He/^{22}Ne$ variations (Fig. 4) can be interpreted as source heterogeneities, namely distinct reservoirs for Fernandina, the Northern Dredges (plumes reservoirs) and the GSC (MORB reservoir) with a specific $^3He/^{22}Ne$ for each reservoir (1, 10 and 20). The Northern dredges value may be the result either of mixing between Fernandina and the MORB reservoir, or of plume heterogeneity. The small variations in the $^3He/^{22}Ne$ ratio and in the neon isotopic composition along the GSC can be the result of a mixture between the plume and MORB components, but one which is difficult to distinguish from shallow level processes such as air contamination and degassing induced fractionation.

For example, samples SOD17-2B and EW69-1 both present a similar $^3He/^{22}Ne_{extrap}$ ratio, but the sample SOD17-2B has higher $^3He/^4He$ ratio and lower $^{21}Ne/^{22}Ne_{extrap}$ isotopic ratios than the sample EW69-1, suggesting a greater plume contribution to this sample (cf. Fig. 3).The increase of the $^3He/^{22}Ne$ ratio north of Fernandina probably reflects the decrease in the plume contribution but additionally a mechanism which fractionates He/Ne is required to explain the data in detail, and these ratios can not be directly interpreted in terms of plume contribution alone.

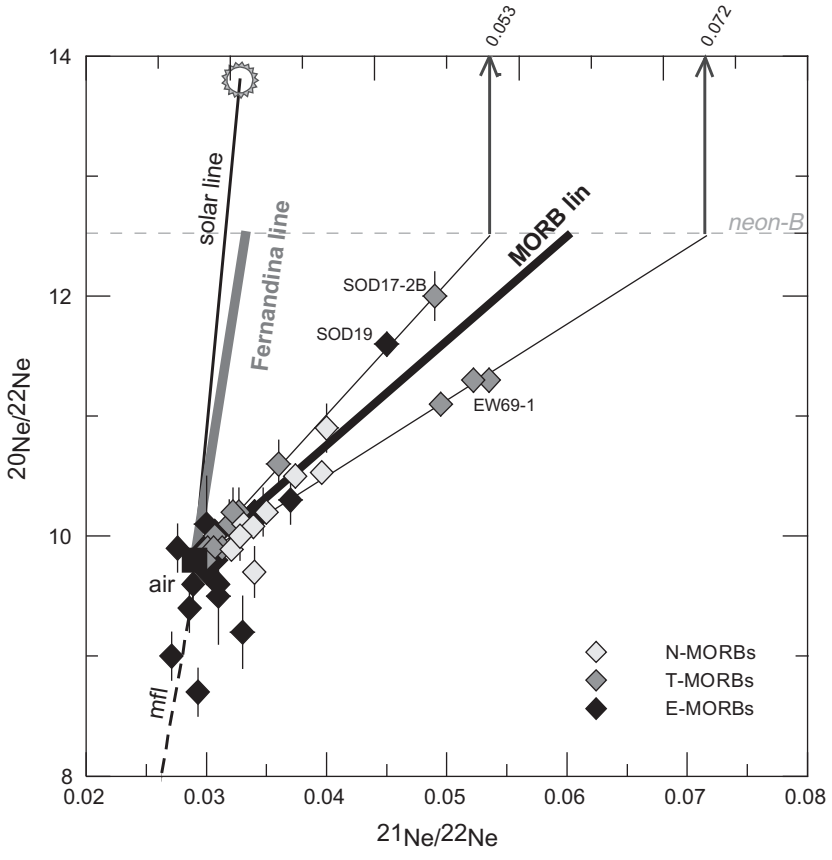

Fig. 2. Neon three isotope diagram showing that the GSC basalt compositions (this study) plot near the MORB-air mixing line (Sarda et al., 1988), far from the plume–air mixing line defined by Fernandina basalts (Kurz et al., 2009). Data are individual step crushing of glassy pillow lavas rims, errors bars are 2σ. mfl is mass fractionation line of atmospheric neon.

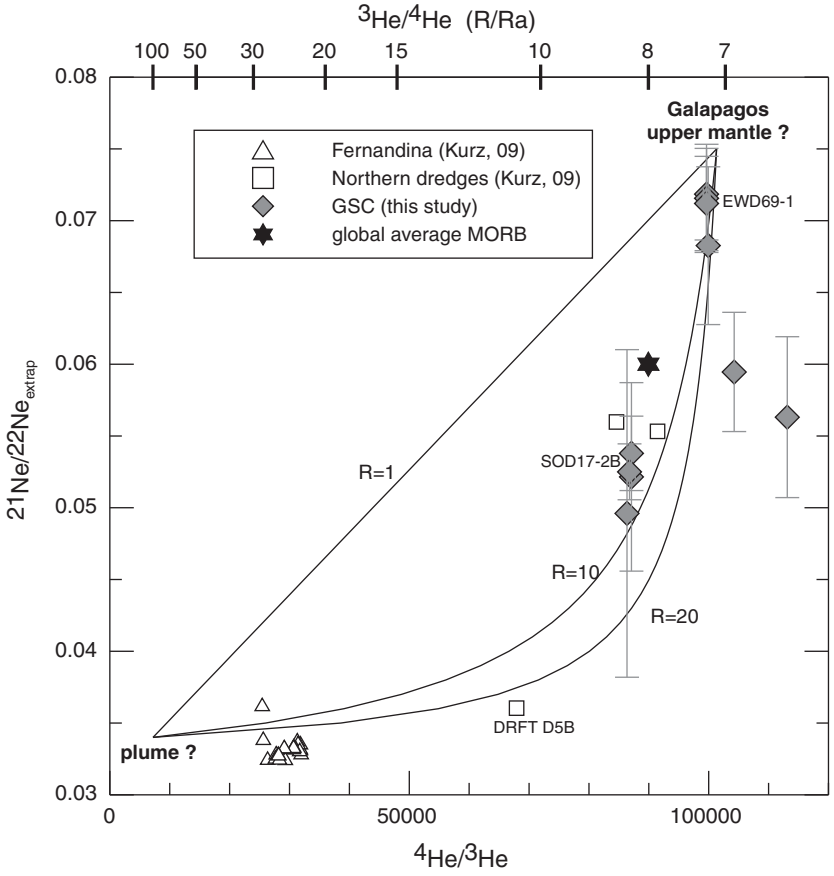

Fig. 3. $^{4}He/^{3}He$ vs. $^{21}Ne/^{22}Ne_{extrap}$ for the GSC (this study – $^{21}Ne/^{22}Ne_{extrap}$ are individual step-crushing, $^{4}He/^{3}He$ are total from crushing) and for Galapagos Islands (Kurz et al., 2009 – $^{21}Ne/^{22}Ne_{extrap}$ and $^{4}He/^{3}He$ are total from crushing or fusion). Mixing lines between assumed MORB and plume end-member compositions are presented for R varying from 1 to 20, where $R = (^{3}He/^{22}Ne)_{MORB}/(^{3}He/^{22}Ne)_{plume}$.

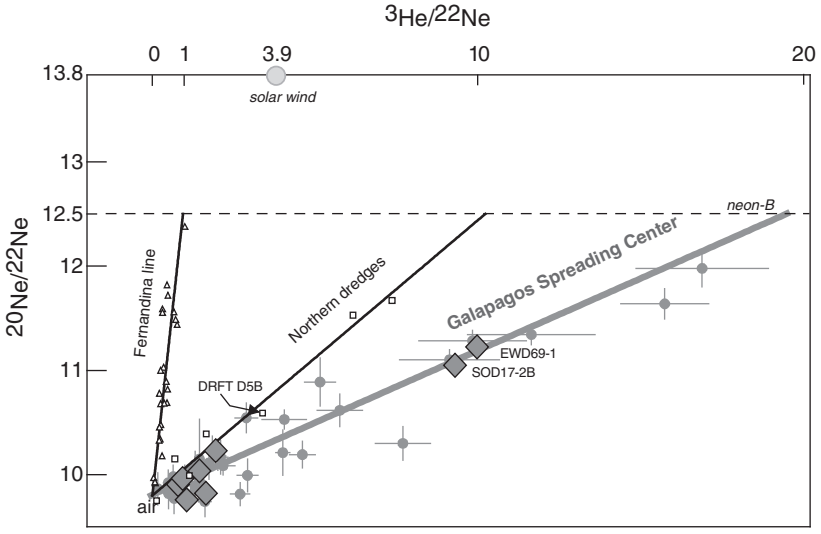

Fig. 4. $^{3}He/^{22}Ne$ vs $^{20}Ne/^{22}Ne$ diagram. Triangles and squares are Fernandina and Northern Dredges, respectively from Kurz et al. (2009); sample totals (fusion or crushing) are plotted. Filled diamonds represent crushing totals obtained on GSC samples (this study) while filled circles represent individual crush steps. ^{3}He content was determined by multiplying ^{4}He content measured in this study by $^{3}He/^{4}He$ ratio measured on the same dredges. For individual steps, $^{3}He/^{4}He$ was considered constant for all the vesicles of a single sample. Errors bars are 2σ.

Furthermore, the $^4He/^{21}Ne^*$ ratios along the GSC, calculated on the samples the least contaminated by atmosphere following the method described in Honda and Patterson (1999) but assuming a primordial neon-B component in Earth's mantle ($^{21}Ne/^{22}Ne = 0.03118$, Trieloff and Kunz, 2005), are between 2.5×10^7 and 1×10^8 and thus are significantly fractionated compared to the production ratio of 2.2×10^7, which suggest the He/Ne ratio is fractionated by a recent mechanism, and is not only the result of mantle heterogeneity. However, as all the samples present highly fractionated ratios, and due to uncertainties in the $^{20}Ne/^{22}Ne$ ratio of the mantle, it's difficult to satisfactorily correct for this recent fractionation in order to calculate the $^3He/^{22}Ne$ ratio of the mantle source.

We note that our $^3He/^{22}Ne_{extrap}$ value of 20 for the MORB samples is not exceptional. $^3He/^{22}Ne$ values (corrected for atmospheric contamination) vary widely in normal MORB samples, between 25 and 70 (Moreira and Sarda, 2000; Sarda and Moreira, 2002). Estimates of the $^3He/^{22}Ne$ ratio for the upper mantle, using the popping rock 2πD43, gives a value of 5 (Moreira et al., 1998) much lower than observed ratios in other MORBs. These higher ratios are generally considered to be due to recent elemental fractionation during magmatic processes (diffusion, degassing, etc.). We conclude that our data are in general consistent with this global view although are towards the lower end of common N-MORB values, with different $^3He/^{22}Ne$ ratios in the MORB and OIB sources (approximately 5 and 1, respectively), but some recent fractionation is required to explain the highest $^3He/^{22}Ne$ ratios in most MORBs, including those of the GSC.

To explain this fractionation, a few mechanisms can be considered. First, the variation could be due to different degrees of incompatibility of He and Ne during melting of the mantle source. However, experimental data suggest helium and neon have approximately the same incompatibility (Brooker et al., 2003). Diffusion during melting would preferentially remove helium from the mantle compared to neon (Burnard, 2004), which would lower the He/Ne ratios, the opposite of the required direction for creating the observed variations. We conclude that the high $^3He/^{22}Ne$ ratio is more probably fractionated by degassing, due to the lower solubility of neon in basaltic melt compared to helium. This is discussed in the following section.

2.2. Degassing along the GSC

As degassing is the major process that affects volatile compositions, knowledge of degassing mechanisms is essential in order to characterise magma source compositions. Degassing in plume influenced ridge sections is more complex than in "normal" ridge sections because there are numerous parameters (bathymetry, AMC depth, degree of fractional crystallisation, magma source and supply, etc.) which vary strongly and can influence degassing processes and intensities.

In this section, we use ^4He–^{40}Ar–CO_2 relative compositions to study degassing processes. When magma rises through the lithosphere, CO_2 becomes over-saturated due to decompression and bubbles nucleate. At equilibrium, noble gases partition between liquid and volatile phases following Henry's law. The initial $^4He/^{40}Ar$ ratio of the mantle can be estimated from the parent (U + Th)/K ratio (considered to be near constant in the mantle). Calculated $^4He/^{40}Ar$ ratios of the mantle are relatively constant (compared to the range observed in MORB glasses), varying between 1 and 3 (Jambon et al., 1985; Staudacher et al., 1989; Burnard et al., 1998). As there are large solubility differences between helium and argon ($K_{He}/K_{Ar} \sim 10$, Carroll and Stolper, 1993), the $^4He/^{40}Ar$ ratio rapidly fractionates during degassing, which makes the $^4He/^{40}Ar$ ratio a good tracer of degassing intensities. In a closed system, the $^4He/^{40}Ar$ ratio in the magma increases up to a maximum equal to the initial $^4He/^{40}Ar^*$ ratio multiplied by the K_{He}/K_{Ar} ratio (~10), while in the volatile phase it tends to the initial magma composition as degree of degassing increases (Moreira and Sarda, 2000; Sarda and Moreira, 2002). In an open system, the ratio increases in both vesicles and magma and there is no maximum limit (Burnard, 1999a). The same principles apply to the $^{40}Ar/CO_2$ ratio, although we do not have independent estimates of the initial ratio, which is also more likely to be variable depending on the magma source (Marty and Zimmermann, 1999). Although vesicle creation and loss will produce open system behaviour, this requires considerable movement of vesicles relative to the magma; this is unlikely given vesicle sizes and magma viscosities (e.g. Bottinga and Javoy, 1990). However, volatile loss will also occur at the interface between liquid magma and solid crust where the partial pressure of CO_2 in the crust will be much lower than that in the magma. Hence a convecting magma chamber will degas volatiles even without creation of vesicles. In this case, the intensity of degassing will depend on the permeability of the crust/magma interface, the magma intrusion morphology (high surface area/volume will increase degassing) and on the Rayleigh number of the magma itself.

During Rayleigh distillation, noble gases fractionate between a volatile phase and the liquid magma following:

$$F_i = F_{CO_2}^{\frac{K_{CO_2}}{K_i}} \tag{1}$$

where F_i is the fraction remaining of gas i in the liquid, F_{CO_2} is the remaining fraction of CO_2 and K_{CO_2} and K_i are, respectively the solubilities of CO_2 and gas i.

As a consequence (Burnard, 1999a):

$$\frac{[Ar]}{[CO_2]} = \left(\frac{[Ar]}{[CO_2]}\right)_0 \times F_{CO_2}^{\frac{K_{CO_2}}{K_{Ar}}-1} \tag{2}$$

and

$$\frac{[He]}{[Ar]} = \left(\frac{[He]}{[Ar]}\right)_0 \times F_{CO_2}^{\frac{K_{CO_2}}{K_{He}}-\frac{K_{CO_2}}{K_{Ar}}} \tag{3}$$

On a logarithm scale, the evolution of the volatile composition of the magma follows a straight line, defined by:

$$\ln\left(\frac{[He]}{[Ar]}\right) = \left(\frac{1-\frac{K_{Ar}}{K_{He}}}{1-\frac{K_{Ar}}{K_{CO_2}}}\right) \times \left[\ln\left(\frac{[CO_2]}{[Ar]}\right) - \ln\left(\frac{[CO_2]}{[Ar]}\right)_0\right] + \ln\left(\frac{[He]}{[Ar]}\right)_0 \tag{4}$$

The evolution along the GSC of the $^4He/^{40}Ar^*$ ratio of the vesicles is presented Fig. 5. The measurements show an increase in $^4He/^{40}Ar^*$ in the plume- influenced zone, which correlates with depth (or the confining pressure on eruption), MgO content (fractional crystallisation) and K_2O/TiO_2 ratio (enrichment of magma source, considered to be a plume tracer). Some samples display particularly high $^4He/^{40}Ar^*$ ratios (maximum 400) indicating that, in the plume influenced zone, degassing occurs in an open system, although this does not automatically preclude a closed system stage (Bottinga and Javoy, 1990; Marty and Zimmermann, 1999; Cartigny et al., 2001).

In a $\ln(^{40}Ar^*/CO_2)$ vs. $\ln(^4He/^{40}Ar^*)$ diagram (Fig. 6), the vesicle compositions of the GSC samples follow a single straight line. The observed trends are consistent with solubility controlled Rayleigh degassing. N-MORB samples are the least degassed, T-MORBs present higher degrees of degassing, followed by E-MORBs which are the most degassed.

We can model the data in order to estimate the relative noble gases abundances of the primary magma, and the percentage of CO_2 lost during degassing. For this model we assume that there is no batch degassing step before the distillation as this step is not necessary to explain the data. We can calculate the composition of the volatiles released during degassing by mass balance. Between two consecutive steps p–1 and p:

$$\left(\frac{CO_2}{Ar}\right)_{\text{released}} = \left(\frac{[CO_2]}{[Ar]}\right)_{p-1} \times \frac{1-\frac{[CO_2]_p}{[CO_2]_{p-1}}}{1-\frac{[Ar]_p}{[Ar]_{p-1}}}$$

$$\text{with}\left(\frac{[Ar]_p}{[Ar]_{p-1}}\right) = \frac{[CO_2]_p}{[CO_2]_{p-1}} \times \frac{\left(\frac{[Ar]}{[CO_2]}\right)_p}{\left(\frac{[Ar]}{[CO_2]}\right)_{p-1}} \quad (5)$$

$$\left(\frac{He}{Ar}\right)_{\text{released}} = \left(\frac{[He]}{[Ar]}\right)_{p-1} \times \frac{1-\frac{[He]_p}{[He]_{p-1}}}{1-\frac{[Ar]_p}{[Ar]_{p-1}}}$$

$$\text{with}\frac{[He]_p}{[He]_{p-1}} = \frac{[CO_2]_p}{[CO_2]_{p-1}} \times \frac{\left(\frac{[He]}{[CO_2]}\right)_p}{\left(\frac{[He]}{[CO_2]}\right)_{p-1}} \quad (6)$$

where subscript "released" indicates the gases that are exsolved from the magma between stages p and p-1. For small steps (we used 1% of CO_2 lost at each step) we can approximate the instantaneous composition of gas released for a given F_{CO_2}

In a $\ln(^{40}Ar^*/CO_2)$ vs. $\ln(^4He/^{40}Ar^*)$ diagram, the evolution of the gases released follows a straight line parallel to, but lying slightly to the right of the evolution of the volatiles dissolved in the magma. Even if the trends for the gas and melt phases are similar, note that the F_{CO_2} implied for a given volatile composition is considerably different for the two phases. For example, $\ln(^4He/^{40}Ar^*)$ of 4 in the gas phase corresponds to 45% CO_2 loss, whereas $\ln(^4He/^{40}Ar^*)$ of 4 in the magma corresponds to only 12% CO_2 lost. As a result, it is necessary to model the data with the previous equations (5 and 6) in order to estimate properly the percentage of CO_2 released during degassing.

The solubility ratios and the initial compositions of the magma (which depend only on the slope and intercept of the magma volatile evolution at equilibrium with the gaseous phase) can be calculated using equation (4).

Fig. 6 presents the model results that best fit our data. The solubility ratios defined by the data are $\frac{K_{He}}{K_{Ar}} = 11$, $\frac{K_{CO_2}}{K_{Ar}} = 5.8$ and $\frac{K_{CO_2}}{K_{He}} = 0.52$, which are in good agreement with literature data. For example, the EIP model of Nuccio and Paonita (2000) (a semi theoretical Extended Ionic Porosity model, which includes the effect of dissolved H_2O and CO_2 on the melt ionic porosity) gives, for the range of GSC compositions and for pressures between 1.2 and 0.5 kbars, $\frac{K_{CO_2}}{K_{He}}$ varying between 0.48 and 0.57 and $\frac{K_{CO_2}}{K_{Ar}}$ varying between 4.2 and 6. At the comparatively low pressures considered here, relative volatile solubilities are not thought to vary significantly from ideal, Henrian behaviour (Sarda and Guillot, 2005), consistent with the observed slopes in Fig. 6.

For an initial $(^4He/^{40}Ar)_0$ ratio of 2, $(CO_2/^{40}Ar)_0$ and $(CO_2/^4He)_0$ are calculated to be $27{,}000 \pm 12\%$ and $13{,}500 \pm 12\%$, respectively. This corresponds to $C/^3He \sim 1.2–1.7 \times 10^9$ (i.e. for $^3He/^4He$ between 8 and 6 Ra within the range expected for normal MORB.

In general, plume material is thought to have $(C/^3He)_0$ higher than N-MORB by about a factor of 4 with correspondingly higher $(CO_2/^4He)_0$ and $(CO_2/^{40}Ar)_0$ (Marty and Zimmermann, 1999), therefore our data are consistent with the hypothesis of little or no Galapagos plume contribution to the volatiles of the GSC basalts; in a $\ln(^{40}Ar^*/CO_2)$ vs. $\ln(^4He/^{40}Ar^*)$ diagram, enriched plume material is expected to lie at lower $^{40}Ar^*/CO_2$ for a given $^4He/^{40}Ar^*$.

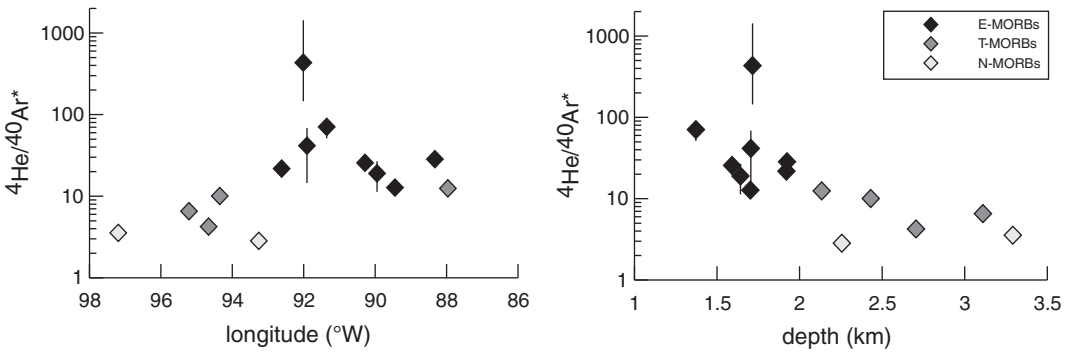

Fig. 5. $^4He/^{40}Ar^*$ variations as a function of the longitude and the eruption depth (totals from crushing)

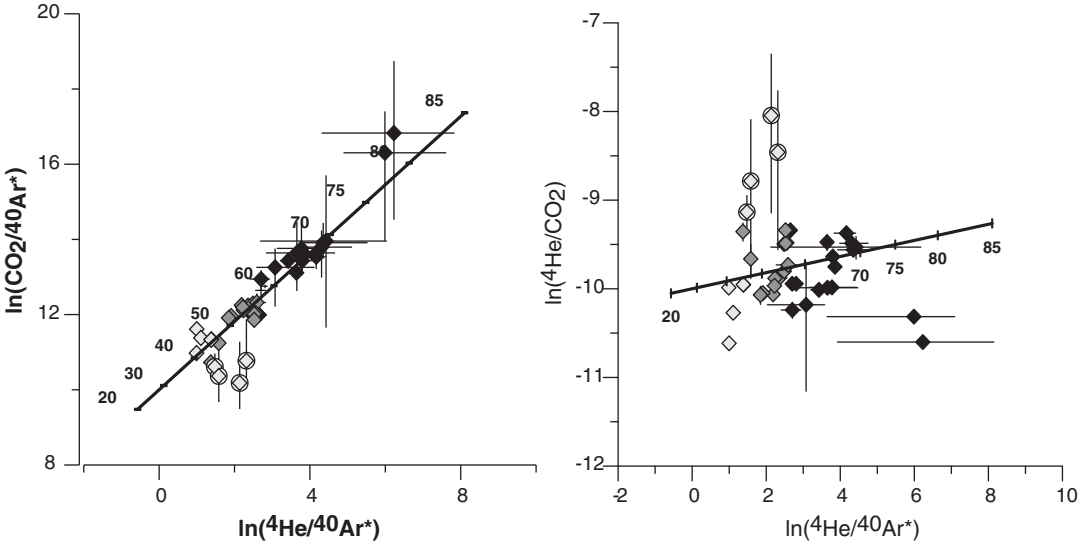

Fig. 6. ln(^{4}He/^{40}Ar*) vs. ln(^{40}Ar*/CO_2) and ln(^{4}He/^{40}Ar*) vs. ln(^{4}He/CO_2) diagram. Symbols are as for Fig. 1. The compositions are consistent with equilibrium degassing processes. Lines represent the modelled volatile phase evolution during Rayleigh distillation of the magma, calculated by mass conservation (see text for details). Numbers along the lines are percent of CO_2 lost from the magma that produces the corresponding instantaneous volatile composition of the gaseous phase. Two samples (SOD3-1B and EWD88-1, circled in black) appear to be CO_2-poor with respect to their noble gas concentrations (i.e. they plot at low CO_2/^{40}Ar* with respect to the correlation line). As these two samples present very low CO_2 content, we interpret these compositions as analytical artefacts, due to CO_2 adsorption on the powder during crushing, which may be important for low CO_2 content (Barker and Torkelson, 1975; Burnard et al., 2002).

The fact that all samples lie on a single slope in Fig. 6, excludes scenarios involving large variations in $(CO_2/^4He)_0$ and $(CO_2/^{40}Ar)_0$.

Our model predicts loss by distillation of at least 40% (N-MORB) up to 70% (more evolved E-MORB) of the initial CO_2 of the magma in order to explain the data. Below, we try to identify factors influencing the degree of degassing in order to improve knowledge of degassing phenomena and to try to constrain the initial CO_2 content of the magma. The degree of degassing correlates with both the depth of eruption (Fig. 5) and with the MgO content of the lavas (Fig. 7). Thus, the extent of degassing could be controlled by either the confining pressure of the overlying seawater during the eruption, or by the degree of fractional crystallisation, as argued by (Marty and Zimmermann, 1999). The interplay between these mechanisms is investigated in the model described below.

The model is based on the fact that when magma crystallises, the CO_2 concentration in the residual liquid increases and when the concentration exceeds CO_2 solubility, degassing occurs (Marty and Zimmermann, 1999). In order to model fractional crystallisation, a realistic composition for the parent magma is required. Starting with a single parental magma composition, although a significant approximation, is justified as we model only major element evolution. We use the "wet" N-MORB parental composition calculated by Eason and Sinton (2006) as a starting composition. This model, performed under pHMELTS, assumes melting by passive adiabatic decompression of the mantle. Fusion starts at 3.07 GPa and the maximum melt fraction is 18% at the base of the crust. The model considers a final crustal thickness of 5.9 km. The parental magma composition calculated by these authors is debatable as the MgO value (17.9 wt.%) is high compared to most models (McKenzie and O'Nions, 1991; Almeev et al., 2008), and the melting rate is at the high end of the range usually considered for MORBs. However, we note that there is little consensus on the MgO content of parental MORB magmas. For example, Falloon et al. (2007) calculate MORB parental liquids by olivine geothermometry with MgO varying between 10% and 16% of MgO. Also, Sours-Page et al. (2002) measure MgO contents of melt inclusion of seamounts lavas on the northern East Pacific Rise up to 12%, indicating the MgO content in the initial magma was higher. Even if the true parental composition on the GSC had a lower MgO content, this will not change the results of our model provided the true parental composition plots along the predicted crystallisation trend. The crystallisation modelled by MELTS by Eason and Sinton (2006) (with 18% MgO for the initial liquid) correctly fits the GSC major element compositions, except for three E-MORBs samples that have MgO lower than 6%, where a different crystallisation trend appears.

In our model, we consider degassing by Rayleigh distillation in the magma chamber during fractional crystallisation (Fig. 7). When magma rises from the AMC to the seafloor, degassing (Rayleigh distillation) is controlled by decompression and not fractional crystallisation. The data should align along the different dotted lines in Fig. 7 depending on their eruption depth.

In order to calculate the initial CO_2 content, we impose the condition that samples at eruption were either at equilibrium or oversaturated with respect to CO_2 (no "under saturation" or "degassing overshoot"). The CO_2 initial concentration of the magma that is in best agreement with the measured ^{4}He/^{40}Ar* is about 250ppm for an initial

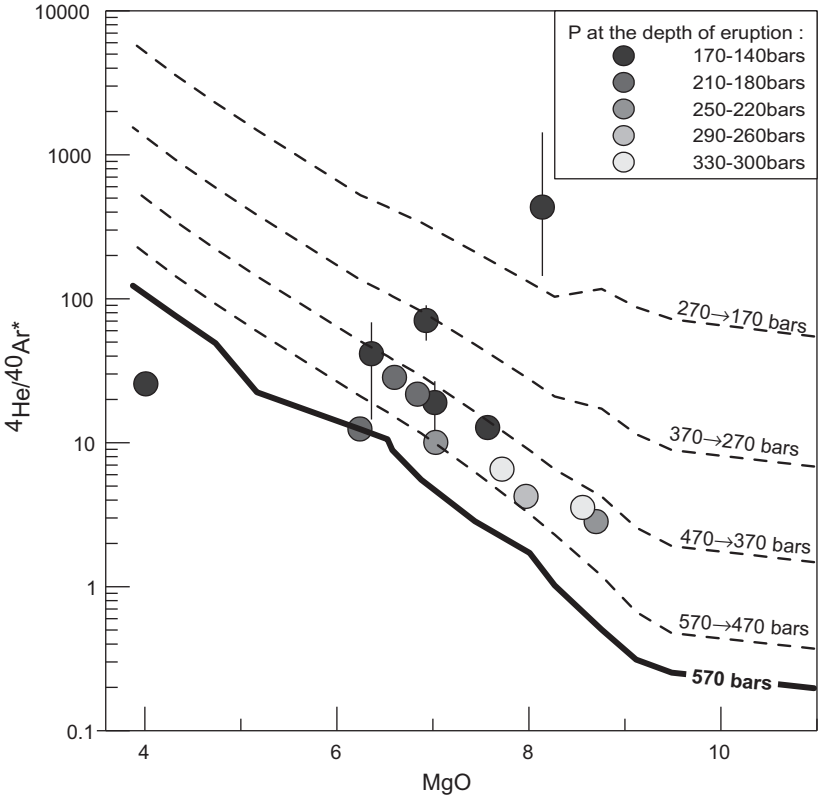

Fig. 7. $^4He/^{40}Ar$ of GSC samples (totals only) plotted as a function of MgO content of the glasses. Symbol shading is a function of the seawater pressure at the depth of eruption, with dark symbols representing shallow eruptions. First of all, model curves were calculated assuming that degassing is forced by fractional crystallisation during residence in the AMC. If no further degassing occurs, the compositions of these magmas are traced by the solid black line. The second stage results from decompression during transfer of magma from the AMC to the seafloor which superimposes degassing on that of the black line. This is traced by the dashed lines where the degree of degassing is governed by the pressure drop indicated on the right hand side of the graph. Both stages are Rayleigh degassing. The pathways have been modelled for AMC pressures of 570 bars (thick lines), corresponding to the pressures for the upper AMC in the plume influenced zone (which has a shallower AMC), but crystallization at 1250 bars (corresponding to the AMC pressure in the least plume-affected portion of the ridge) gives similar compositions. The initial magma composition is from Eason and Sinton (2006) (GSC N-MORB with 17.9% MgO; see text for details). Isobaric fractional crystallisation was calculated using MELTS (Graham, 2002; Ghiorso and Sack, 1995; Asimow and Ghiorso, 1998) with temperature steps of 5°C. The C solubility used (0.137 ppm/bar) is from Jendrzejewski et al. (1997). Noble gas solubilities were calculated using the EIP model of Nuccio and Paonita (2000). CO_2 contents increase in the liquid during crystallisation. When the CO_2 concentration in the liquid exceeds solubility, gaseous CO_2 is produced and noble gases partition between gas and liquid depending on their solubilities; volatile phase compositions were calculated by mass balance at each crystallisation step. Magma subsequently rises from the AMC to the seafloor without crystallisation, and during this step degassing is controlled only by decompression causing CO_2 solubility decrease.

MgO = 17.9%; 350ppm is required if the initial magma had MgO = 9%. Considering CO_2 as highly incompatible during melting, this requires a mantle source with CO_2 concentrations of ~45 ppm (1×10^{-6} mol/g) (considering 18% of partial fusion for MgO = 17.9% or about 13% of partial fusion for a MgO = 9%). This value is entirely consistent with independent estimates of the mantle carbon content. Marty and Tolstikhin (1998) estimated a CO_2 content of $(3.1 \pm 1.9) \times 10^{-6}$ mol/g for the upper mantle (50–150 ppm) (calculated from $^3He/CO_2$ ratio and considering 10% of partial melting at the origin of the MORB) while Saal et al. (2002), using CO_2/Nb ratio, estimate the CO_2 content of the upper mantle at 72 ± 19 ppm. However, all these estimates (including our own) are lower than those of Cartigny et al. (2008) who estimate a content of about 220 ppm (considering partial fusion of the mantle of 12%).

From Fig. 7 we can see the GSC compositions plot between the model predictions for the AMC pressure (570 bars) and for the pressure at eruption depth. Similar results (not shown) are obtained for models run with crystallisation at 1250 bars (the AMC depth in non-plume influenced regions of the ridge). In general, sample compositions are parallel to the predicted curves in Fig. 7, but their compositions do not necessarily agree with the confining pressure at eruption. A possible explanation of this is that the T and E-MORB samples may not be in equilibrium with their liquids at the confining seawater pressure at eruption, i.e. the liquids are partially oversaturated. The oversaturations required to account for the data are in the range of 1–3, which correspond to measured oversaturations in natural glasses (Dixon et al., 1988; Jendrzejewski et al., 1997).

2.3. Influence of degassing on neon relative abundances

As discussed above, the He/Ne ratio is also sensitive to degassing. Variations in $^{3}He/^{22}Ne$ (the range of ratios calculated for the samples least contaminated by atmosphere is 10–23) seems to correlate with $^{4}He/^{40}Ar^{*}$ and $^{40}Ar^{*}/CO_2$ (not shown) along the ridge. This is consistent with fractionation by degassing although we note that the relative solubilities have to be adjusted in order that the slope of the degassing trend matches the model with the neon solubility closer to that of the argon compared to experimentally determined solubilities. Adjusting solubilities has already been proposed by Moreira and Sarda (2000) to explain MORB and OIB degassing trends. With the adjusted solubilities, the degassing model is consistent with a starting $^{3}He/^{22}Ne$ ratio of the magma close to the popping rock ratio and a $^{4}He/^{21}Ne^{*}$ ratio equal to the mantle production ratio. However, significant atmospheric contamination increases uncertainties and reduces the sample $^{3}He/^{22}Ne_{extrap}$ database therefore it is difficult to use the data to constrain the degassing scenario. The lack of consensus on the $^{20}Ne/^{22}Ne$ ratio of the mantle adds further uncertainties.

2.4. Creating a helium-free plume signature on the GSC

Previous Pb–Sr–Nd isotopic data require a ≈30 percent contribution of plume material to the GSC at 91°W (Schilling et al., 2003). Although the Galapagos plume is likely to be heterogeneous (Kurz and Geist, 1999; Schilling et al., 2003), any plume source is expected to be volatile-rich compared to the MORB source region. It is surprising therefore that even considering an heterogeneous Galapagos plume there is no obvious plume contribution to the GSC volatiles given that the lithophile tracers (Sr, Nd, Pb, REE, K/Ti, etc.) and the water contents all reflect the presence of such a component within the GSC basalts. Geist et al. (2005) proposed that melting on the margins of a thermal plume could explain the absence of a plume signal in the He isotope systematics of Wolf Island (which lies between the GSC and the Galapagos Islands; Fig. 1) and hence on the GSC: volatile depletion during this melting event would result in a predominantly MORB source volatile signature on the GSC (and Wolf Island). However, it is difficult to imagine a melting model could explain the extremely efficient separation of silicates and volatiles that is required in this scenario because: a) very low partition coefficients for the noble gases and CO_2 during this melting event are implied (volatile partition coefficients need to be significantly lower than *any* lithophile trace element, which is inconsistent with experimental data (Heber et al., 2007)); and b) extremely low partial melt fractions would be necessary in order to fractionate volatiles from incompatible lithophile elements. Even generation of a carbonatitic melt is unlikely to produce the required fractionation: Burnard et al. (2010) demonstrate that the noble gases are not particularly soluble in carbonatite liquids, therefore immiscible separation of a carbonatitic phase is unlikely to significantly affect the noble gas concentration of the silicate phase.

Schilling et al., 2003) propose that the Pb–Hf–Nd–Sr anomalies observed in the Galapagos Islands and along the GSC are due the presence of ancient recycled oceanic crust in the plume producing the characteristic HIMU signature. If this HIMU component were spatially separated from the high $^{3}He/^{4}He$, Fernandina-type component within the plume (i.e the plume was heterogeneous) and the HIMU portion of the plume was preferentially sampled by the GSC, then this could explain the decoupling between the volatile signature (He, Ne, Ar, CO_2) and Pb–Hf–Nd–Sr isotopes observed on the GSC. At Fernandina island samples are a mixture of the high $^{3}He/^{4}He$ plume and HIMU components, and thus present elevated $^{3}He/^{4}He$ ratios and HIMU isotopic signatures. Considering oceanic crust is largely degassed of mantle volatiles, its' volatile content will be dominated by seawater (equilibrated with the atmosphere), which will be modified by radiogenic production (^{21}Ne, ^{40}Ar and ^{4}He) over time. Could incorporation of a HIMU component (with recycled Ne and Ar) account for the low $^{40}Ar/^{36}Ar$ and low $^{20}Ne/^{22}Ne$ ratios observed at 90–92°W on the GSC? Recycling of noble gases to the mantle is controversial: while recycling of heavy noble gases (Ar, Xe) has been proposed (Sarda et al 1999; Holland and Ballentine 2006) a) this has never been suggested for Ne and b) it has been shown that Ar recycling is not required in order to explain Ar isotope data of oceanic basalts (Burnard, 1999b). In fact, along the GSC, $^{40}Ar/^{36}Ar$ does correlate, albeit poorly, with plume indicators (K/Ti, etc., not shown). However, as pointed out by Burnard (1999b), this does not confirm a recycled origin for the low $^{40}Ar/^{36}Ar$ ratios: the K/Ti maximum coincides with the most shallow portions of the ridge. This is also where most atmospheric contamination will occur because the confining pressure at eruption is lowest. As elsewhere, it is not possible to demonstrate that there is no recycling of Ar in the HIMU source of the Galapagos plume, but at the same time the data can readily be explained without such recycling. Thus an heterogeneous plume is a plausible hypothesis which accounts for the GSC lava compositions yet we note that HIMU – type volcanism is often associated with elevated $C/^{3}He$ ratios (Marty and Zimmermann, 1999) which is not observed in the $CO_2/^{3}He$ in these samples (there is no maximum observed at 91°W).

An alternative explanation which can account for the apparent decoupling between volatile and lithophile element behaviour along the GSC is loss of volatiles from a plume-derived melt *prior to mixing with the GSC magma*. If the plume melts with sufficiently low partial melt fraction then (a) the C concentration will be high in the melt, and (b) the melt will not be extracted from the mantle. Owing to the high C concentration, this melt will degas at relatively high pressures (see below). Thus, volatile and lithophile signatures are "decoupled" by creation and loss of a volatile phase and not by fractionation during the melting process. In this way, it is possible to create a melt that has the lithophile characteristics of the plume but essentially be devoid of the noble gases and CO_2. This model also neatly explains how there is a plume-derived H_2O signature observed on the GSC: water, being much more soluble than CO_2 or the noble gases (Dixon et al., 1995), will not be depleted to the same extent (as CO_2, for example) during the volatile-loss event. Although it may seem that the highly

fractionated volatile signatures around 91 W on the GSC are compatible with this mechanism (i.e. the fractionated $^4He/^{40}Ar^*$ and $CO_2/^{40}Ar^*$ ratios observed in the plume affected region of the GSC are the residue of the formation of the discrete gas phase within the plume) this is not in fact possible: our postulated degassed plume endmember will be characterised by high $^4He/^{40}Ar^*$ and high $^3He/^4He$ ratios. If the high $^4He/^{40}Ar^*$ ratios observed on the GSC originated from this degassed plume endmember, then clearly the He would have to also come from this endmember (because this endmember has high $^4He/^{40}Ar^*$). Helium, being the most soluble noble gas in silicate melts, will have the highest concentration (of the noble gases) in the postulated degassed plume component. Any plume contribution will, therefore, be more evident in the He isotope signature than the other isotope systems (Ne, Ar). There is no mixing scenario which can produce low $^3He/^4He$ ratios with high $^4He/^{40}Ar^*$ (as observed on the GSC) during mixing between MORB-type volatiles and the degassed plume postulated above. We have to conclude that the volatiles in the GSC are dominated by those from the MORB source and the high $^4He/^{40}Ar^*$ result from late stage degassing as discussed in section 4.

This mechanism implies the creation and then loss of a discrete gas phase relatively deep within the mantle, prior to arrival of the plume at the melting zone of the GSC. From surface wave tomography, Villagomez et al. (2007) image a high velocity "lid" that is located at a depth of around 40 km in the vicinity of the ridge. This lid is underlain by a northward shoaling, low velocity zone interpreted by Villagómez et al. to be hotter (by 30–150° C) plume material that may contain up to 0.5% melt, i.e. insufficient liquid for efficient melt extraction. However, at such low partial melt fractions, incompatible element concentrations, including CO_2, would be elevated; CO_2 concentrations of the order of several percent are to be expected in 0.5% partial melts. For example, if the plume source prior to melting contains four times more C than the MORB source (=50 ppm) which would be the minimum C concentration implied by $C/^3He$ systematics (Marty and Zimmermann, 1999), then a 0.5% partial melt implies 4% CO_2 in the melt. Experiments by Pan et al (1991) and Jendrzejewski et al. (1997) both predict that CO_2 solubility at 40 km (11 kbar) is ≈0.8 wt.% CO_2. Quite clearly, C solubility in such a melt could be exceeded at high pressure, resulting in the formation of a noble gas rich, independent CO_2 phase. This phase would be able to separate from the silicate liquid and escape the system. The result is a "residue" (which nevertheless contains silicate melt) which continues to the ridge.

3. CONCLUSIONS

This study shows that there are only very minor contributions of volatiles from the Galapagos plume, as characterised by Fernandina Island, to the volatile signature observed on the Galapagos Spreading Center. Firstly, neon isotopic ratios are indistinguishable from MORB values and are unlike the neon isotope signature of Fernandina and secondly, all GSC samples degas along the same trend requiring that all GSC magmas had the same initial volatile content. This excludes a volatile-rich source region (such as would be expected at sites of plume–ridge interaction) along the GSC. This is in contrast with "lithophile" element tracers such as the isotopes of Pb, Sr, Nd, REE contents, K/Ti ratios and even H_2O concentrations whose signatures require that enriched material from the Galapagos plume reach the GSC. We propose that the volatile and lithophile element compositions on the GSC can be explained by either (1) the plume degassing at depth before mixing below the GSC with the normal MORB source, or (2) the plume component containing unradiogenic helium and neon is not involved at the GSC, but the enriched lithophile isotopic compositions are due to melting of some recycled oceanic crust (HIMU signature) carried by the plume.

Loss of volatiles on the GSC, which in some ridge sections is extensive, follows Rayleigh distillation with the extent of degassing being controlled by a combination of fractional crystallisation and eruption depth. However, although there is a correlation between extent of degassing and eruption depth, some CO_2 oversaturation is nevertheless required to explain the He–Ar–CO_2 relative abundances.

ACKNOWLEDGEMENTS

Bernard Marty is warmly thanked for input and discussions. We thank John Lupton for access to the helium isotope lab in Newport, OR, which is supported by the NOAA Vents program. DG was supported by the Marine Geology & Geophysics program of the National Science Foundation. We are grateful to David Hilton, Mark Kurz and Philippe Sarda for their constructive reviews. This is CRPG contribution n° 2099.

REFERENCES

Almeev R., Holtz F., Koepke J., Haase K. and Devey C. (2008) Depths of partial crystallization of H_2O-bearing MORB: phase equilibria simulations of basalts at the MAR near Ascension Island (7–11S). *Journal of Petrology* **49**, 25–45.

Asimow P. and Ghiorso M. (1998) Algorithmic modifications extending MELTS to calculate subsolidus phase relations. *American Mineralogist* **83**, 1127–1131.

Barker C. and Torkelson B. E. (1975) Gas adsorption on crushed quartz and basalt. *Geochimica et Cosmochimica Acta* **39**, 212–218.

Bottinga Y. and Javoy M. (1990) MORB degassing: bubble growth and ascent. *Chemical Geology* **81**, 255–270.

Breddam K., Kurz M. D. and Storey M. (2000) Mapping out the conduit of the Iceland mantle plume with helium isotopes. *Earth and Planetary Science Letters* **176**, 45–55.

Brooker R. A., Du Z., Blundy J. D., Kelley S. P., Allan N. L., Wood B. J., Chamorro E. M., Wartho J. A. and Purton J. A. (2003) The 'zero charge' partitioning behaviour of noble gases during mantle melting. *Nature* **423**, 738–741.

Burnard P. (1999a) The bubble-by-bubble volatile evolution of two mid-ocean ridge basalts. *Earth and Planetary Science Letters* **174**, 199–211.

Burnard P. (1999b) Origin of argon–lead isotopic correlation in basalts. *Science* **286**, 871.

Burnard P. (2004) Diffusive fractionation of noble gases and helium isotopes during mantle melting. *Earth and Planetary Science Letters* **220**, 287–295.

Burnard P. G., Farley K. A. and Turner G. (1998) Multiple fluid pulses in a Samoan harzburgite. *Chemical Geology* **147**, 99–114.

Burnard P. G., Graham D. W. and Farley K. A. (2002) Mechanisms of magmatic gas loss along the Southeast Indian Ridge and the Amsterdam – St. Paul Plateau. *Earth and Planetary Science Letters* **203**, 131–148.

Burnard P., Toplis M. J. and Medynski S. (2010) Low solubility of He and Ar in carbonatitic liquids: implications for decoupling noble gas and lithophile isotope systems. *Geochimica et Cosmochimica Acta* **74**, 1672–1683.

Canales J. P., Ito G., Detrick R. S. and Sinton J. (2002) Crustal thickness along the western Galápagos Spreading Center and the compensation of the Galápagos hotspot swell. *Earth and Planetary Science Letters* **203**, 311–327.

Carroll M. R. and Stolper E. M. (1993) Noble gas solubilities in silicate melts and glasses: new experimental results for argon and the relationship between solubility and ionic porosity. *Geochimica et Cosmochimica Acta* **57**, 5039–5051.

Cartigny P., Jendrzejewski N., Pineau F., Petit E. and Javoy M. (2001) Volatile (C, N, Ar) variability in MORB and the respective roles of mantle source heterogeneity and degassing: the case of the Southwest Indian Ridge. *Earth and Planetary Science Letters* **194**, 241–257.

Cartigny P., Pineau F., Aubaud C. and Javoy M. (2008) Towards a consistent mantle carbon flux estimate: insights from volatile systematics (H_2O/Ce, [delta]D, CO_2/Nb) in the North Atlantic mantle (14 N and 34 N). *Earth and Planetary Science Letters* **265**, 672–685.

Christie D. M., Werner R., Hauff F., Hoernle K. and Hanan B. B. (2005) Morphological and geochemical variations along the eastern Galápagos Spreading Center. *Geochem. Geophys. Geosyst.* **6.**

Cushman B., Sinton J., Ito G. and Eaby Dixon J. (2004) Glass compositions, plume–ridge interaction, and hydrous melting along the Galápagos Spreading Center, 90.5°W to 98°W. *Geochem. Geophys. Geosyst.* **5**.

Detrick R. S., Sinton J. M., Ito G., Canales J. P., Behn M., Blacic T., Cushman B., Dixon J. E., Graham D. W. and Mahoney J. J. (2002) Correlated geophysical, geochemical, and volcanological manifestations of plume–ridge interaction along the Galápagos Spreading Center. *Geochem. Geophys. Geosyst.* **3.**

Dixon J. E., Stolper E. and Delaney J. R. (1988) Infrared spectroscopic measurements of CO_2 and H_2O in Juan de Fuca Ridge basaltic glasses. *Earth and Planetary Science Letters* **90**, 87–104.

Dixon J. E., Stolper E. M. and Holloway J. R. (1995) An experimental study of water and carbon dioxide solubilities in mid-ocean ridge basaltic liquids part I: calibration and solubility models. *Journal of Petrology* **36**, 1607–1631.

Eason D. and Sinton J. (2006) Origin of high-Al N-MORB by fractional crystallization in the upper mantle beneath the Galápagos Spreading Center. *Earth and Planetary Science Letters* **252**, 423–436.

Falloon T. J., Danyushevsky L. V., Ariskin A., Green D. H. and Ford C. E. (2007) The application of olivine geothermometry to infer crystallization temperatures of parental liquids: Implications for the temperature of MORB magmas. *Chemical Geology* **241**, 207–233.

Fisk M. R., Bence A. E. and Schilling J. G. (1982) Major element chemistry of Galápagos Rift Zone magmas and their phenocrysts. *Earth and Planetary Science Letters* **61**, 171–189.

Geist D. J., Naumann T. R., Standish J. J., Kurz M. D., Harpp K. S., White W. M. and Fornari D. J. (2005) Wolf volcano, Galápagos Archipelago: melting and magmatic evolution at the margins of a mantle plume. *Journal of Petrology* **46**, 2197–2224.

Ghiorso M. S. and Sack R. O. (1995) Chemical mass transfer in magmatic processes IV. A revised and internally consistent thermodynamic model for the interpolation and extrapolation of liquid–solid equilibria in magmatic systems at elevated temperatures and pressures. *Contributions to Mineralogy and Petrology* **119**, 197–212.

Graham D. W. (2002) Noble gas isotope geochemistry of mid-ocean ridge and ocean island basalts: characterization of mantle source reservoirs. *Reviews in Mineralogy and Geochemistry* **47**, 247–317.

Graham D. W., Christie D. M., Harpp K. S. and Lupton J. E. (1993) Mantle plume helium in submarine basalts from the galápagos platform. *Science* **262**, 2023–2026.

Graham D. W., Larsen L. M., Hanan B. B., Storey M., Pedersen A. K. and Lupton J. E. (1998) Helium isotope composition of the early Iceland mantle plume inferred from the Tertiary picrites of West Greenland. *Earth and Planetary Science Letters* **160**, 241–255.

Heber V. S. and Brooker R. A., et al. (2007) Crystal-melt partitioning of noble gases (helium, neon, argon, krypton, and xenon) for olivine and clinopyroxene. *Geochimica et Cosmochima Acta* **71**(4), 1041–1061.

Holland G. and Ballentine C. J. (2006) Seawater subduction controls the heavy noble gas composition of the mantle. *Nature* **441**(7090), 186–191.

Honda M. and Patterson D. B. (1999) Systematic elemental fractionation of mantle-derived helium, neon, and argon in mid-oceanic ridge glasses. *Geochimica et Cosmochimica Acta* **63**, 2863–2874.

Ito G. and Lin J. (1995) Oceanic spreading center–hotspot interactions: constraints from along-isochron bathymetric and gravity anomalies. *Geology* **23**, 657–660.

Ito G. and Lin J., et al. (2003) Observational and theoretical studies of the dynamics of mantle plume-mid-ocean ridge interaction. *Review of Geophysics* **41**, 1017.

Jambon A., Weber H. W. and Begemann F. (1985) Helium and argon from an Atlantic MORB glass: concentration, distribution and isotopic composition. *Earth and Planetary Science Letters* **73**, 255–268.

Javoy M. and Pineau F. (1991) The volatiles record of a "popping" rock from the Mid-Atlantic Ridge at 14 N: chemical and isotopic composition of gas trapped in the vesicles. *Earth and Planetary Science Letters* **107**, 598–611.

Jendrzejewski N., Trull T. W., Pineau F. and Javoy M. (1997) Carbon solubility in Mid-Ocean Ridge basaltic melt at low pressures (250–1950 bar). *Chemical Geology* **138**, 81–92.

Kurz M. D. and Geist D. (1999) Dynamics of the Galápagos hotspot from helium isotope geochemistry. *Geochimica et Cosmochimica Acta* **63**, 4139–4156.

Kurz M. D., Meyer P. S. and Sigurdsson H. (1985) Helium isotopic systematics within the neovolcanic zones of Iceland. *Earth and Planetary Science Letters* **74**, 291–305.

Kurz M. D., Moreira M., Curtice J., Lott Iii D. E., Mahoney J. J. and Sinton J. M. (2005) Correlated helium, neon, and melt production on the super-fast spreading East Pacific Rise near 17 S. *Earth and Planetary Science Letters* **232**, 125–142.

Kurz M. D., Curtice J., Fornari D., Geist D. and Moreira M. (2009) Primitive neon from the center of the Galápagos hotspot. *Earth and Planetary Science Letters* **286**, 23–34.

Marrocchi Y., Burnard P. G., Hamilton D., Colin A., Pujol M., Zimmermann L. and Marty, B. (2009) Neon isotopic measurements using high-resolution, multicollector noble gas mass spectrometer: HELIX-MC. *Geochem. Geophys. Geosyst.* **10.**

Marty B. and Tolstikhin I. N. (1998) CO_2 fluxes from mid-ocean ridges, arcs and plumes. *Chemical Geology* **145**, 233–248.

Marty B. and Zimmermann L. (1999) Volatiles (He, C, N, Ar) in mid-ocean ridge basalts: assessment of shallow-level fractionation and characterization of source composition. *Geochimica et Cosmochimica Acta* **63**, 3619–3633.

McKenzie D. A. N. and O'Nions R. K. (1991) Partial melt distributions from inversion of rare earth element concentrations. *Journal of Petrology* **32**, 1021–1091.

Moore J. G. (1979) Vesicularity and CO_2 in mid-ocean ridge basalt. *Nature* **282**, 250–253.

Moreira M. and Sarda P. (2000) Noble gas constraints on degassing processes. *Earth and Planetary Science Letters* **176**, 375–386.

Moreira M., Kunz J. and Allègre C. (1998) Rare gas systematics in popping rock: isotopic and elemental compositions in the upper mantle. *Science* **279**, 1178–1181.

Moreira M., Breddam K., Curtice J. and Kurz M. D. (2001) Solar neon in the Icelandic mantle: new evidence for an undegassed lower mantle. *Earth and Planetary Science Letters* **185**, 15–23.

Niedermann S., Bach W. and Erzinger J. (1997) Noble gas evidence for a lower mantle component in MORBs from the southern East Pacific Rise: decoupling of helium and neon isotope systematics. *Geochimica et Cosmochimica Acta* **61**, 2697–2715.

Nuccio P. M. and Paonita A. (2000) Investigation of the noble gas solubility in H_2O–CO_2 bearing silicate liquids at moderate pressure II: the extended ionic porosity (EIP) model. *Earth and Planetary Science Letters* **183**, 499–512.

Pan V. and Holloway J. R., et al. (1991) The pressure and temperature dependence of carbon dioxide solubility in tholeiitic basalt melts. *Geochimica et Cosmochimica Acta* **55**, 1587–1595.

Saal A. E., Hauri E. H., Langmuir C. H. and Perfit M. R. (2002) Vapour undersaturation in primitive mid-ocean-ridge basalt and the volatile content of Earth's upper mantle. *Nature* **419**, 451–455.

Sarda P. and Moreira M. (2002) Vesiculation and vesicle loss in mid-ocean ridge basalt glasses: He, Ne, Ar elemental fractionation and pressure influence. *Geochimica et Cosmochimica Acta* **66**, 1449–1458.

Sarda P. and Guillot B. (2005) Breaking of Henry's law for noble gas and CO_2 solubility in silicate melt under pressure. *Nature* **436**, 95–98.

Sarda P., Staudacher T. and Allègre C. J. (1988) Neon isotopes in submarine basalts. *Earth and Planetary Science Letters* **91**, 73–88.

Sarda P., Moreira M. and Staudacher T. (1999) Argon–lead isotopic correlation in Mid-Atlantic Ridge Basalts. *Science* **283**, 666–668.

Schilling J.-G., Anderson R. N. and Vogt P. (1976) Rare earth, Fe and Ti variations along the Galapagos spreading centre and their relationship to the Galápagos mantle plume. *Nature* **261**, 108–113.

Schilling J. G., Kingsley R. H. and Devine, J. D. (1982) Galápagos Hot Spot-Spreading Center System 1. Spatial petrological and geochemical variations (83°W–111°W). *J. Geophys. Res.* **87**.

Schilling J.-G., Fontignie D., Blichert-Toft J., Kingsley R. and Tomza, U. (2003) Pb-Hf-Nd-Sr isotope variations along the Galápagos Spreading Center (101–83°W): Constraints on the dispersal of the Galápagos mantle plume. *Geochem. Geophys. Geosyst.* **4**.

Sours-Page R., Nielsen R. L. and Batiza R. (2002) Melt inclusions as indicators of parental magma diversity on the northern East Pacific Rise. *Chemical Geology* **183**, 237–261.

Starkey N. A., Stuart F. M., Ellam R. M., Fitton J. G., Basu S. and Larsen L. M. (2009) Helium isotopes in early Iceland plume picrites: Constraints on the composition of high $^3He/^4He$ mantle. *Earth and Planetary Science Letters* **277**, 91–100.

Staudacher T., Sarda P., Richardson S. H., Allègre C. J., Sagna I. and Dmitriev L. V. (1989) Noble gases in basalt glasses from a Mid-Atlantic Ridge topographic high at 14 N: geodynamic consequences. *Earth and Planetary Science Letters* **96**, 119–133.

Trieloff M. and Kunz J. (2005) Isotope systematics of noble gases in the Earth's mantle: possible sources of primordial isotopes and implications for mantle structure. *Physics of The Earth and Planetary Interiors* **148**, 13–38.

Verma S. P. and Schilling, J.-G. (1982) Galápagos hot spot-Spreading Center System 2. $^{87}Sr/^{86}Sr$ and large ion lithophile element variations (85°W–101°W). *J. Geophys. Res.* **87**.

Verma S. P., Schilling J.-G. and Waggoner D. G. (1983) Neodymium isotopic evidence for Galápagos hotspot-spreading center system evolution. *Nature* **306**, 654–657.

Villagomez D. R., Toomey D. R., Hooft E. E. E. and Solomon, S. C. (2007) Upper mantle structure beneath the Galápagos Archipelago from surface wave tomography. *Journal of Geophysics Research* **112.**

Yatsevich I. and Honda M. (1997) Production of nucleogenic neon in the Earth from natural radioactive decay. *Journal of Geophysics Research* **102**, 10291–10298.

Yokochi R. and Marty B. (2004) A determination of the neon isotopic composition of the deep mantle. *Earth and Planetary Science Letters* **225**, 77–88.

Associate editor: Richard J. Walker